

# High precision determination of chiral indices of electron diffraction patterns from carbon nanotubes

Davis Brown

Physics Department, University of North Carolina at Chapel Hill.

May 8, 2020

UNC Honor Pledge: I, Davis Brown, certify that no unauthorized assistance has been received or given in the completion of this work

# 1 Abstract

The chiral indices that define the structure of a carbon nanotube can be precisely and automatically determined with deep learning. This work introduces a program for the simulation of the diffraction patterns of carbon nanotubes, which can be analytically expressed using the diffraction theory for helices. A convolutional neural network architecture is proposed to process diffraction pattern images of carbon nanotubes and determine the chiral indices of the nanotube. The model determines the chiral indices of the carbon nanotube with greater than 98% accuracy on the test set of simulated diffraction patterns. The geometry and diffraction theory of carbon nanotubes is also introduced.

# Contents

<b>1 Abstract</b>	<b>2</b>
<b>2 Introduction</b>	<b>4</b>
<b>3 Preliminary CNT Geometry</b>	<b>4</b>
3.1 Carbon nanotube introduction and definitions . . . . .	4
3.2 Positions of atoms in the radial projection . . . . .	6
<b>4 Diffraction from carbon nanotubes</b>	<b>7</b>
4.1 The scattering amplitude . . . . .	7
4.2 Electron diffraction from a continuous helix . . . . .	7
4.3 Electron diffraction from a nanotube . . . . .	8
4.4 Selection rule . . . . .	8
4.5 Determination of chiral indices with the principal layer lines . . . . .	9
<b>5 Algorithm for the determination of chiral indices</b>	<b>10</b>
5.1 Deep learning in crystallography . . . . .	10
5.2 Description of the data set . . . . .	10
5.3 Data augmentation . . . . .	11
5.4 Architecture description for the tandem models . . . . .	11
5.5 Model training and results . . . . .	11
<b>6 Conclusion</b>	<b>12</b>
<b>7 Appendix</b>	<b>13</b>
<b>8 Acknowledgements</b>	<b>14</b>

## 2 Introduction

In 1993, Sumio Iijima discovered single-wall carbon nanotubes (SWNTs), only two years after his observation of multiwall carbon nanotubes (MWNTs) with a transmission electron microscope [1, 2]. The discovery and study of carbon nanotubes generated intense interest, in no small part because of their remarkable and promising properties. Carbon nanotubes have high ultimate tensile strength. The tensile strength of SWNTs are as high as 20 times that of steel and the tensile strength for MWNTs was measured at  $\approx 150$  GPa from an electric arc [3, 4].

Importantly, the helical structure of SWNTs has a strong influence on its electronic state. A single-wall carbon nanotube can be described by wrapping (i.e. rolling) a graphene sheet with a certain cut. The diameter and chirality (the helicity, where we define where the sheet is rolled-up) of the carbon nanotube can be uniquely defined given its chiral indices  $(n,m)$ . Because of the configuration of the conduction and the valence bands of graphene, some SWNTs are semi-conducting and some are metal-conducting [5]. Knowledge of the chiral indices  $(n,m)$  gives whether the nanotube is semiconducting or metallic.

Transmission electron microscopy (TEM) has been used to effectively characterize the structure of carbon nanotubes. With electron diffraction, the chiral indices, and thus the atomic structure, of a carbon nanotube can be found [6]. The kinematic diffraction theory for carbon nanotubes was given by Qin in 1994 [7, 8]. Interestingly, the formulation is based on the mathematics and language developed for the groundbreaking helical theory for DNA molecules [9, 10, 11]. Namely, the theories connect the real three-dimensional helical structures with the diffraction patterns in reciprocal space with the Fourier transform of a discrete helix [12].

We give an overview of some of the preliminary geometry used for carbon nanotubes. We then describe the kinematic diffraction theory based on work from Lu-Chang Qin [7, 8]. We offer a new platform for the simulation of diffraction patterns of carbon nanotubes given its chiral indices. We then describe a deep learning architecture and diffraction image processing pipeline to precisely determine the chiral indices of a carbon nanotube from a diffraction image. Namely, we hope that this can be developed into a tool to accurately and quickly determine the structure of carbon nanotubes.

## 3 Preliminary CNT Geometry

### 3.1 Carbon nanotube introduction and definitions

We can gain a schematic geometric understanding of SWNTs by considering a single atomic layer of graphene. Graphene is a sheet of  $sp^2$ -bonded carbon atoms in a hexagonal crystal lattice. In real space, the lattice is spanned by basis vectors  $\vec{a}_1$  and  $\vec{a}_2$ , illustrated in Fig. 1. We can express the basis in Cartesian coordinates,

$$\vec{a}_1 \equiv \frac{\sqrt{3}}{2} a_0 \vec{x} + \frac{a_0}{2} \vec{y}, \quad \vec{a}_2 \equiv \frac{\sqrt{3}}{2} a_0 \vec{x} - \frac{a_0}{2} \vec{y}, \quad (1)$$

where  $a_0 = |\vec{a}_1| = |\vec{a}_2| = \sqrt{3}a_{C-C} \simeq \sqrt{3} \times 0.142$  nm = 0.246 nm and  $a_{C-C} = 0.142$  nm is the carbon-carbon bond length of graphene. It is worth noting that the basis is not orthogonal, with  $\vec{a}_1 \cdot \vec{a}_2 = \frac{a_0^2}{2}$ . Similarly, we can write the reciprocal space vectors from the real space basis as

$$\vec{a}_1^* = \frac{2}{3a_0^2} (2\vec{a}_1 - \vec{a}_2), \quad \vec{a}_2^* = \frac{2}{3a_0^2} (-\vec{a}_1 + 2\vec{a}_2). \quad (2)$$

We define the perimeter vector, or chiral vector, in terms of the real crystallographic basis,

$$\vec{A} = (n, m) = n\vec{a}_1 + m\vec{a}_2, \quad (3)$$

where typically  $(0 \leq |m| \leq n)$ . Fig. 1 gives the schematic for the perimeter vector of  $\vec{A} = (6, 3)$ . The magnitude of (3),

$$|\vec{A}| = a_0 (n^2 + m^2 + nm)^{1/2}, \quad (4)$$

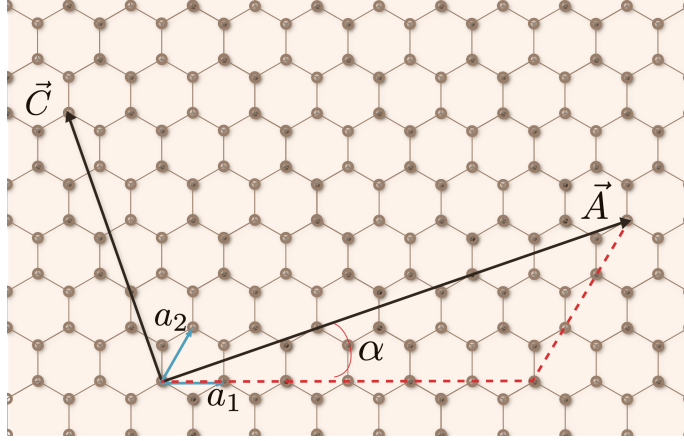


Figure 1: Schematic diagram of a graphene mesh. The basis vectors  $\vec{a}_1$  and  $\vec{a}_2$  are separated by an angle of  $60^\circ$ . The helical angle  $\alpha$  is the angle between the basis vector  $\vec{a}_1$  and the chiral vector  $\vec{A}$ . For this example, the perimeter vector  $\vec{A} = (6, 3)$  and the tube axis, which is orthogonal to the perimeter vector, is  $\vec{C} = (-4, 5)$ .

is the circumference of the tube, from which we can obtain the diameter by  $d = |\vec{A}|/\pi$ . We also define a helical angle  $\alpha$  as the angle between the basis vector  $\vec{a}_1$  and the chiral vector  $\vec{A}$  [6],

$$\cos \alpha = \frac{\vec{A} \cdot \vec{a}_1}{|\vec{A}| |\vec{a}_1|} = \frac{2n + m}{2\sqrt{n^2 + m^2 + nm}}. \quad (5)$$

We can use (5) to calculate the  $\alpha$  in Fig. 1, where  $\vec{A} = (6, 3)$ , as  $\alpha \approx 19.107^\circ$ . It is worth noting that there are three ways that graphene can be rolled into a tube:

- 1) Chiral nanotube: where  $0^\circ < |\alpha| < 30^\circ$
- 2) Zig-zag nanotube: where  $m = 0$ , i.e.  $\alpha = 0^\circ$
- 3) Armchair nanotube: where  $n = m$ , i.e.  $\alpha = 30^\circ$ ,

where we have ignored the handedness of the tube and assigned a chiral angle between  $0^\circ$  and  $30^\circ$ . The tube axis,  $\vec{C}$ , is orthogonal to the perimeter vector. We can express the indices of the tube axis by enforcing orthogonality,

$$(n, m) \cdot (n_c, m_c) = 0, \quad (6)$$

so

$$\implies \frac{n_c}{m_c} = -\frac{n + 2m}{2n + m}, \quad (7)$$

where the indices  $(n_c, m_c)$  are chosen such that their only common divisor is 1. We can express the periodicity,  $c$ , of the carbon nanotube along its axis [6, 13],

$$c = a_0 \sqrt{n_c^2 + m_c^2 + n_c m_c} = \frac{\sqrt{3}a_0}{M} \sqrt{n^2 + m^2 + nm} = \frac{\sqrt{3}A}{M}, \quad (8)$$

where  $M$  is defined by

$$M \equiv \gcd(2m + n, 2n + m), \quad (9)$$

with  $\gcd$  denoting the greatest common divisor.

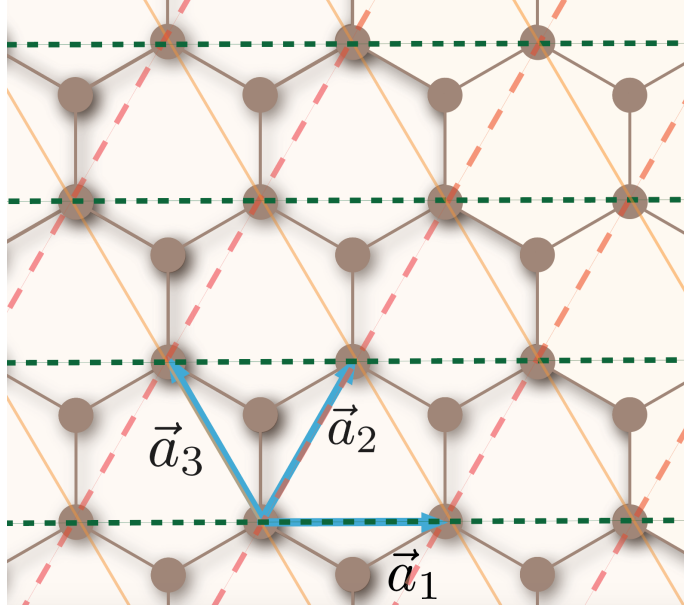


Figure 2: A radial projection schematic of the three equivalent molecular helices (each with a pair of carbon atoms) parallel to  $\vec{a}_1$ ,  $\vec{a}_2$ , and  $\vec{a}_3$ . Adopted from [6].

### 3.2 Positions of atoms in the radial projection

The atomic positions can also be expressed as pairs of parallel atomic helices with coordinates  $(x_j, z_j)$  in the radial projection [6]. A helpful schematic of how a radial project represents a helix with chirality (14, 1) is given in the Appendix [14]. As shown in Fig. 2, there are three equivalent helices, parallel to the crystallographic basis vectors  $\vec{a}_1$ ,  $\vec{a}_2$ , and  $\vec{a}_3 = \vec{a}_2 - \vec{a}_1$ . [6, 8] defines the atomic positions for each equivalent helix. For brevity, we give the atomic positions for the primary and secondary helices parallel to  $\vec{a}_1$ . The primary helix is defined as the carbon atoms directly intersected by the lines on the radial projection parallel to the basis vectors (in Fig. 2, the atoms on the green dashed line parallel to the width of the paper compose the primary helix for  $\vec{a}_1$ ). The secondary helix is made up the carbon atoms in the pair offset from its pair atom in the primary helix by a translation vector  $(\Delta x_0^{(i)}, \Delta z_0^{(i)})$ , where  $i = 1, 2$ , or  $3$  corresponding to the basis vectors. There are  $m$  helix pairs parallel with  $\vec{a}_1$ . Referencing Fig. 2, the coordinates of the primary helix pair to  $\vec{a}_1$  are given by

$$x_j^{(1,0)} = ja_0 \cos(\alpha) \quad (10)$$

$$z_j^{(1,0)} = -ja_0 \sin(\alpha), \quad (11)$$

where  $j = 0, 1, 2, \dots, n + m - 1$ , as there are  $n + m$  atoms parallel to  $\vec{a}_1$ . The atomic position of the atoms on the secondary helix is simply the primary helix defined by (10) and (11) offset by the translation vector  $(\Delta x_0^{(1)}, \Delta z_0^{(1)})$ ,

$$x_j^{(1,1)} = x_j^{(1,0)} + \Delta x_0^{(1)}, \quad (12)$$

$$z_j^{(1,1)} = z_j^{(1,0)} + \Delta z_0^{(1)}, \quad (13)$$

where

$$\Delta x_0^{(1)} = \frac{a_0}{\sqrt{3}} \cos(30^\circ + \alpha), \quad (14)$$

$$\Delta z_0^{(1)} = -\frac{a_0}{\sqrt{3}} \sin(30^\circ + \alpha). \quad (15)$$

## 4 Diffraction from carbon nanotubes

### 4.1 The scattering amplitude

This section serves mostly as a summary of [6, 7, 8]. We describe the electron diffraction from SWNTs, and how we can determine the chiral indices from the diffraction pattern. In the first Born approximation, the differential cross section of a wave is given by

$$\frac{d\sigma}{d\Omega} = |F(\vec{q})|^2 = \left| \sum_j f_j(q) e^{2\pi i \vec{q} \cdot \vec{r}_j} \right|^2, \quad (16)$$

where  $\vec{q}$  is the scattering vector for atoms at positions  $\vec{r}_j$ ,  $f_j(q)$  is the atomic form factor, and  $F(\vec{q})$  is the scattering amplitude. The density of the scattering centers is related to the amplitude with a Fourier transform. Note, however, that there is a 'phase problem' that makes the structure of the atoms difficult to obtain. Namely, with the measurement of the diffracted intensity  $I(\vec{q})$ , we lose the information of the phase,  $\varphi(\vec{q})$ , from the complex scattering amplitude, where  $F(\vec{q}) = \sqrt{I(\vec{q})} e^{i\varphi(\vec{q})}$ , or

$$I(\vec{q}) = |F(\vec{q})|^2. \quad (17)$$

For convenience, we rewrite (16) as [7]

$$F(\vec{q}) = \int V(\vec{r}) \exp(2\pi i \vec{q} \cdot \vec{r}) d\vec{r}, \quad (18)$$

where the scattering vector  $|\vec{q}| = 2 \sin(\Theta/2)/\lambda$ , where  $\Theta$  is the total scattering angle and  $\lambda$  is the electron wavelength, and

$$V(\vec{r}) = \left( \frac{2\pi m e}{h^2} \right) U(\vec{r}), \quad (19)$$

where  $U(\vec{r})$  is the Coulomb potential of the scattering object, where  $m$  is the electron's relativistic mass,  $h$  is the Planck constant, and  $-e$  is the charge of the electron.

### 4.2 Electron diffraction from a continuous helix

Because the carbon nanotube is a helix, we find it useful to rewrite (18) in polar coordinates  $(r, \phi, z)$ , relating to Cartesian coordinates with

$$\begin{aligned} x &= r \cos(\phi) \\ y &= r \sin(\phi) \\ z &= z \end{aligned}$$

and for the coordinates in reciprocal space with

$$\begin{aligned} X &= R \cos(\Phi) \\ Y &= R \sin(\Phi) \\ Z &= Z \end{aligned}$$

The structure factor in polar coordinates is then

$$F(R, \Phi, l) = \frac{1}{c} \sum_{n=-\infty}^{+\infty} \exp \left[ in \left( \Phi + \frac{\pi}{2} \right) \right] \int_0^c \int_0^{2\pi} \int_0^\infty V(r, \phi, z) J_l(2\pi r R) \exp \left[ i \left( \frac{2\pi l z}{c} - n\phi \right) \right] r dr d\phi dz, \quad (20)$$

where the object has period  $c$  along  $z$ , and where we have used the Jacobi-Anger identity to express plane waves in terms of cylindrical waves,

$$\exp(iu \cos \phi) = \sum_{n=-\infty}^{+\infty} J_n(u) \exp \left[ i n \left( \phi + \frac{\pi}{2} \right) \right]. \quad (21)$$

The full derivation of (20) is given in [15]. For a right-handed continuous helix with a radius  $r_0$  and pitch length  $P$ , the scattering potential is expressed by

$$V(r, \phi, z) = V_0 \delta(r - r_0) \delta \left( \frac{2\pi z}{P} - \phi \right). \quad (22)$$

With this potential, we obtain the scattering amplitude [7]

$$F(R, \Phi, l) = r_0 V_0 J_l(2\pi r_0 R) \exp \left[ i \left( \Phi + \frac{\pi}{2} \right) l \right], \quad (23)$$

and this is the celebrated equation obtained Cochran, Crick, and Vand in their formulation of X-ray diffraction patterns for synthetic polypeptides, which played a crucial role for the discovery of the double helix structure of DNA [15, 16]. For a continuous helix, the distribution for the intensity, using (17) and (23), is

$$I(R, \Phi, l) = |F(R, \Phi, l)|^2 \propto [J_l(2\pi r_0 R)]^2. \quad (24)$$

### 4.3 Electron diffraction from a nanotube

For a discontinuous helix with carbon atoms located at discrete positions along its radius, we discretize (20) and sum over  $j$  atoms in a cell and the  $n$  integers given by the selection rule derived in 4.4,

$$F(R, \Phi, l) = \sum_h \exp \left[ ih \left( \Phi + \frac{\pi}{2} \right) \right] J_h(2\pi r_0 R) \sum_j f_j \exp \left[ i \left( \frac{2\pi l z_j}{c} - h\phi_j \right) \right], \quad (25)$$

which we rewrite as

$$F(R, \Phi, l) = \sum_h \exp \left[ ih \left( \Phi + \frac{\pi}{2} \right) \right] J_h(2\pi r_0 R) \times \sum_j f_j \exp \left[ 2\pi i \left( \frac{hx_j}{A} + \frac{lz_j}{c} \right) \right], \quad (26)$$

where  $A$  is the magnitude of the perimeter, and  $(x_j, z_j)$  are the coordinates from the radial projection defined in (10-11) [6]. Note that the first exponential term and the first order Bessel function in (26) accounts for the curvature and contributes the Bessel function to the diffraction peaks. The second exponential term contributes the diffraction pattern from the hexagonal graphene mesh.

### 4.4 Selection rule

We can express the selection rule for helical diffraction by considering the discrete helix as a product of a continuous helix, with structural periodicity  $c$  and pitch length  $P$ , and a set of planes with spacing  $\Delta$ . The allowed reflections for a layer line  $l$  are [6]

$$l = ht + kp, \quad (27)$$

where  $t = c/P$  is the turns per periodicity and  $p = c/\Delta$  is the scattering objects per periodicity for the helix. From the geometry defined for the helix parallel to  $\vec{a}_1$ , we can calculate  $C$  and  $\Delta$  in terms of the chiral indices  $(n, m)$ . We can then solve for  $t$  and  $p$  in (27). Substituting these solutions back into (27), we obtain the selection rule for a nanotube,

$$l = h \frac{2n + m}{Mm} + k \frac{2(n^2 + m^2 + nm)}{Mm}. \quad (28)$$

Working in the radial projection basis with atomic helix pairs parallel to the crystallographic basis vectors, we can substitute the selection rule for a nanotube (28) into the structure factor (26) to find the structure factor for a carbon nanotube, given in [6].

For a SWNT, there are three principal pairs of layer lines with respective members of the pairs above and below the central, equatorial, line. These are formed from the three primary Miller indices for graphene, (01), ( $\bar{1}0$ ), and (11). The graphene reflections form the layer lines labeled  $l_1$ ,  $l_2$ , and  $l_3$ , respectively. The layer lines have respective spacings  $D_1$ ,  $D_2$ , and  $D_3$ . We will use these layer lines for the determination of the chiral indices of a carbon nanotube.

For each layer line for a given chiral indices  $(n, m)$ , there is almost always one dominant Bessel function. From the selection rule, the order  $h$  of the allowed Bessel functions for a layer line is given by

$$h = h_0 + \frac{2K(n^2 + m^2 + nm)}{M}, \quad (29)$$

where  $h_0$  is the smallest non-negative integer for the layer line, and  $K$  are positive integers such that  $h$  is an integer [6]. Further, if we consider the allowed Bragg reflections for the graphene lattice and the crystallographic indices of the graphene reflections, we can obtain the relation

$$h = h_0 n + k_0 m \quad (30)$$

where  $(h_0 k_0)$  give the graphene reflection [17]. Given the Miller indices for each layer line and the relation (30), we determine the dominant Bessel function for each layer line. For  $l_1$  with Miller indices (01), the order of the dominant Bessel function is

$$h = (0) * n + (1) * m = m,$$

$h = -n$  for  $l_2$  with Miller indices ( $\bar{1}0$ ), and  $h = n + m$  for  $l_3$  with Miller indices (11).

#### 4.5 Determination of chiral indices with the principal layer lines

With (17) and (24), we find

$$\begin{aligned} I_{l1}(R) &\propto |J_m(\pi dR)|^2, \\ I_{l2}(R) &\propto |J_{-n}(\pi dR)|^2, \\ I_{l3}(R) &\propto |J_{n+m}(\pi dR)|^2. \end{aligned} \quad (31)$$

Likewise, the layer line spacing distance from the equatorial line is found with trigonometry,

$$\begin{aligned} D_1 &= a^* \cos(\alpha), \\ D_2 &= a^* \cos(60^\circ - \alpha), \\ D_3 &= a^* \cos(60^\circ + \alpha). \end{aligned} \quad (32)$$

where  $a^*$  is the magnitude of the reciprocal basis vector.

We created software that produces simulated diffraction images for SWNTs with supplied chiral indices  $(n, m)$  from equations (31) and (32). See Fig. 3 for example output of four different pairs of chiral indices.

Using the relation for the helical angle  $\alpha$  and (32),

$$\alpha = \tan^{-1} \left( \frac{2D_2 - D_1}{\sqrt{3}D_1} \right). \quad (33)$$

The ratio of chiral indices is found with (5) and (32),

$$\frac{m}{n} = \frac{2D_2 - D_1}{2D_1 - D_2}. \quad (34)$$

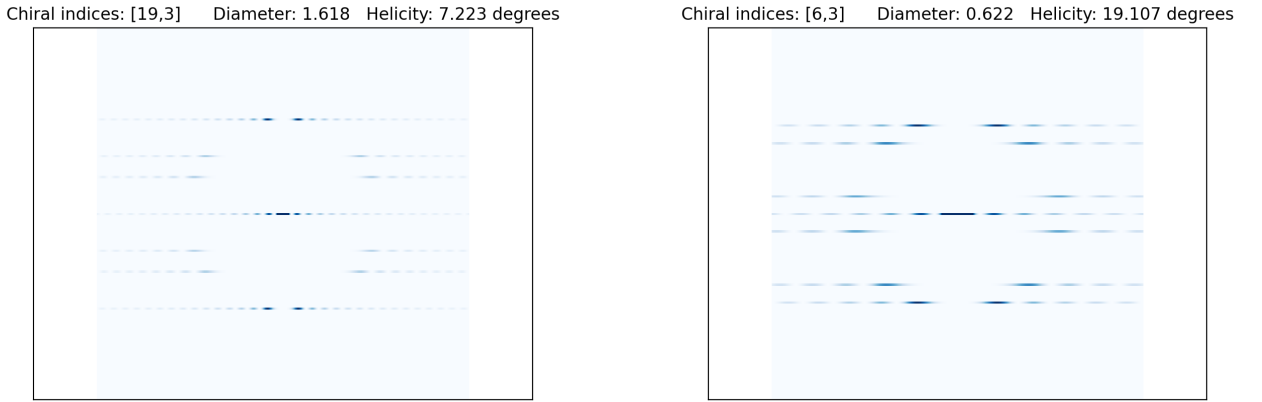


Figure 3: Simulated diffraction patterns of the layer lines  $l_0, l_1, l_2$  and  $l_3$  for single-wall carbon nanotubes with chiral indices (19, 11) and (6, 3).

For our determination of the chiral indices, we use (34). While we obtain only a ratio of the chiral indices and cannot discern beyond an equivalence class of chiral indices  $(jn_0, jm_0)$  for positive integer  $j$ , finding the ratio  $m/n$  has important advantages. First, determining the correct dominant order of Bessel function is computationally expensive with. An  $\ell^2$  norm or a general Hough transform has to differentiate between many possible orders of Bessel functions. Determining a layer line takes far less information as all we need is (qualitatively) a roughly consistent line. The ratio method is also more robust to noise compared to matching Bessel functions [6].

## 5 Algorithm for the determination of chiral indices

### 5.1 Deep learning in crystallography

Deep learning techniques have had remarkable success across many fields, and have seen some limited success in crystallography [18, 19, 20, 21, 22]. Machine learning algorithms typically leverage large data sets to learn representations of a feature space. A promising approach within crystallography is to simulate diffraction patterns to make a large data set, and train a model on the data set in order to predict information about the phase and structure of diffraction patterns. This approach has seen success in e.g. phase identification in powder X-ray diffraction with near 100% accuracy of the identification of certain inorganic compounds [20].

### 5.2 Description of the data set

We produce a small data set of simulated single-wall carbon nanotube diffraction images using the analytic descriptions given in (31) and (32) with chiral indices inclusively up to (150, 150), totalling

$$C_{151}^{(2)} = \binom{151 + 2 - 1}{2} = 11,476 \text{ images.} \quad (35)$$

The pixel distances of the layer lines from the equatorial line are used to generate the simulated images, so the data set comes already labeled.



Figure 4: A single example augmented image from the SWNT diffraction pattern data set with chiral indices (75,4) randomly rotated by 31.2°.

### 5.3 Data augmentation

The simulated diffraction pattern images are augmented with random rotations to simulate the real diffraction orientations of carbon nanotubes. While the patterns are shown mapped to a blue intensity in the accompanying web application, we map the diffraction pattern images in the data set to gray scale to more closely match real intensity data. Gaussian noise is added to simulate the noise present in transmission electron microscopy [21]. An example augmented image is shown in Fig. 4. The simulated diffraction pattern images had dimension 512x512.

### 5.4 Architecture description for the tandem models

We use a pair of deep convolutional neural network (CNN) models. The first model identifies the position of the equatorial line  $l_0$  in a diffraction pattern. The second model identifies the spacing of the layer lines  $l_1$  and  $l_2$  in order to find the ratio of chiral indices defined in (34). We adopted the architecture from Lee et. al. [23]. In brief, we parameterize a line segment for the image with  $(x_s, y_s, x_e, y_e)$ . We then employ a VGG16 [24] with 13 convolutional layers and two pooling layers, shown in Fig. 5. The final regression layer is the regression loss function

$$L_{\text{reg}}(\vec{l}_p, \vec{l}) = \sum_{i=1}^4 L_2(l_{p,i} - \vec{l}_i), \quad (36)$$

where  $\vec{l}_p$  is the proposed line segment,  $\vec{l}$  is the ground truth line segment (there are multiple loss outputs for the second architecture), and  $L_2$  is the  $\ell^2$  norm. We uniformly sample lines  $(x_s, y_s, x_e, y_e)$  for the input image. The first model outputs only a single proposed equatorial line  $l_0$ . The second model outputs four proposed lines for the layer lines  $l_1$  and  $l_2$ . We implement the models and train the architecture with the machine learning framework PyTorch [25]. The code for the deep learning model will be provided along with the simulation software code.

### 5.5 Model training and results

The data set is given a 70/30 training vs test split, where 8,033 randomly selected diffraction pattern images are used to train the model, and 3,442 images are used to test the model. The training set is further divided

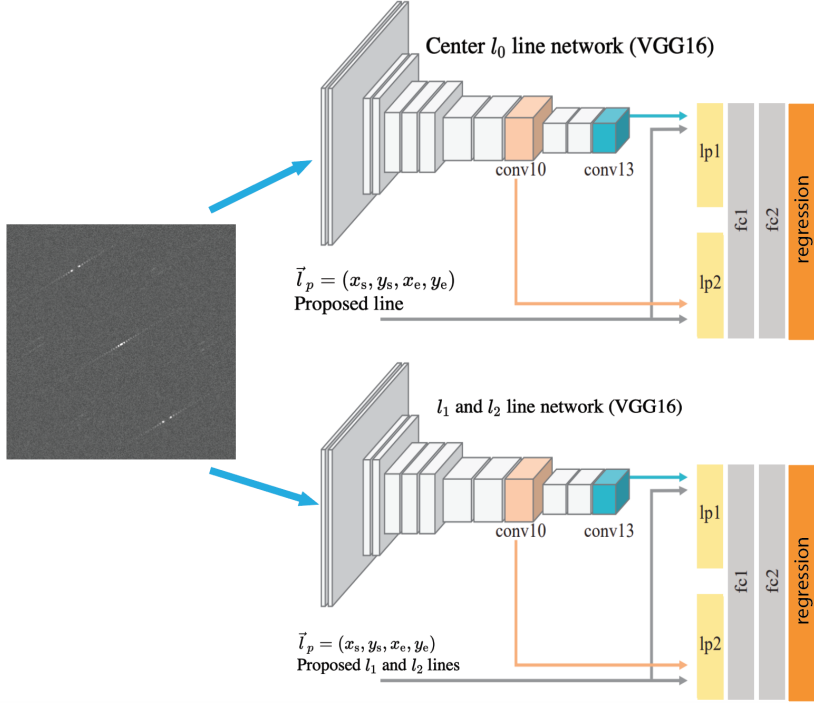


Figure 5: A schematic of the two CNN model architectures to identify the layer lines. For both the Center line network and the  $l_1/l_2$  line network, the input diffraction image passes through 13 convolutional layers, two line pooling layers, and then to two fully connected layers respectively. The output for the center line network is a single equatorial line parameterized by  $(x_s, y_s, x_e, y_e)$ . The output for the  $l_1/l_2$  line network is four such lines corresponding to the line spacing needed in (34). Adopted from [23].

into a 90/10 training vs validation split, where 7,229 images are used for training and 803 images are used for validation of the model during training. During training, we use a batch size of 64 images and a learning rate  $\epsilon = 0.001$ .

We found that the model identified 7,890 of the 8,033 test simulated diffraction pattern images correctly for an accuracy of 98.21%. One example output for the diffraction pattern given in Fig. 4 (pulled arbitrarily from the test set) is given in Fig. 6. Despite the high testing accuracy for the determination of chiral indices, it is worth noting that we did use simulated, rather than real, diffraction patterns for the training, validation, and testing.

## 6 Conclusion

We built software to simulate the diffraction patterns of single-wall carbon nanotubes, which were analytically re-derived in this write-up. We propose a deep learning algorithm and architecture for the precise determination of the chiral indices of carbon nanotubes from diffraction. We found that our model performed very well on the test simulated data, with accuracy over 98%. The model still needs to be tested on laboratory diffraction patterns to ensure that it can precisely determine the chiral indices from real data.

Future work should include formulating uncertainty for the proposed chiral indices ratio  $m/n$ . While we currently output a loss for the output line given by (36) as well as the loss for the next closest proposed lines, this uncertainty should be formulated to propose the next most likely pair of chiral indices (given ratio  $m/n$ ) as well. A similar set of model architectures may also be used to potentially learn the chiral indices  $(n, m)$  directly from the intensity profile of the layer lines. This architecture was only implemented because of its

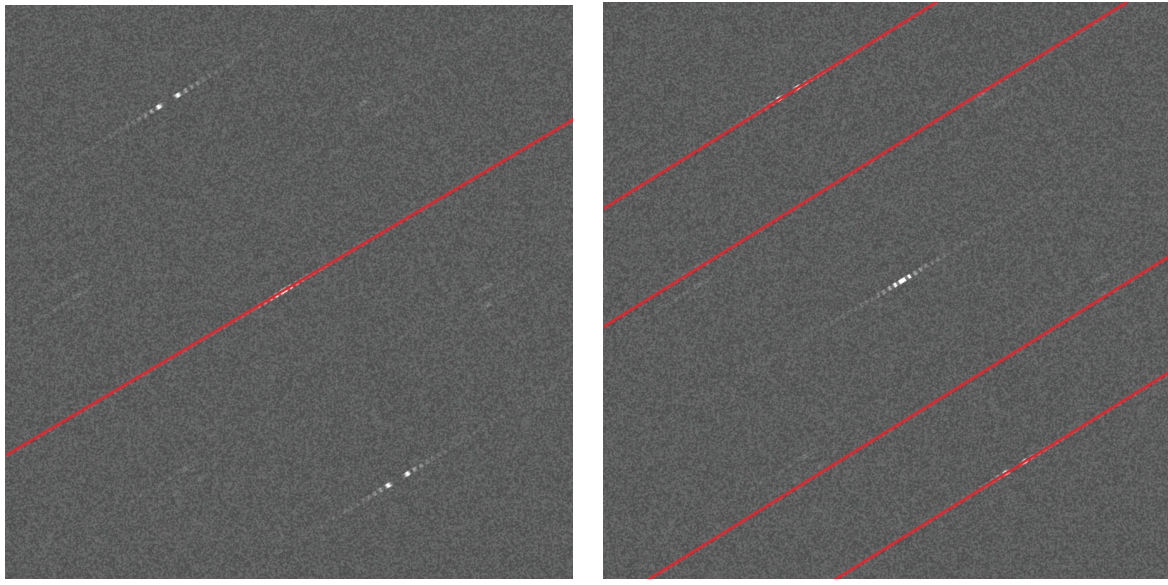


Figure 6: The center line of best fit and the  $l_1$  and  $l_2$  lines of best fit for the respective architectures. The ratio of chiral indices for the SWNT with chirality of (75,4) was correctly identified as 4/75.

relative straightforwardness; it is likely the more precise determination will directly use the Bessel function.

## 7 Appendix

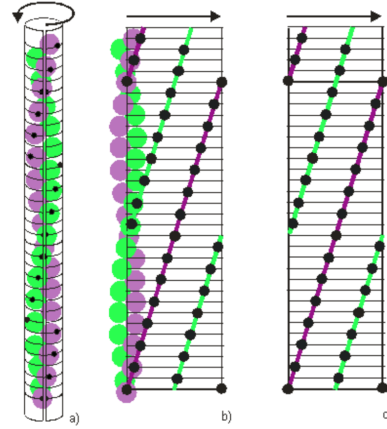


Figure 7: (Appendix) An explanation of a radial projection for a helix with chirality (14,1). Adopted from [14].

## 8 Acknowledgements

This work was supported by Professor Lu-Chang Qin in PHYS 395 as well as the Department of Physics at the University of North Carolina at Chapel Hill. I would like to express my appreciation for the great deal of time Professor Qin gave this semester.

## References

- [1] Sumio Iijima. Helical microtubules of graphitic carbon. *Nature*, 354(6348):56–58, 1991.
- [2] Sumio Iijima and Toshinari Ichihashi. Single-shell carbon nanotubes of 1-nm diameter. *Nature*, 363(6430):603–605, 1993.
- [3] Min-Feng Yu, Oleg Lourie, Mark J Dyer, Katerina Moloni, Thomas F Kelly, and Rodney S Ruoff. Strength and breaking mechanism of multiwalled carbon nanotubes under tensile load. *Science*, 287(5453):637–640, 2000.
- [4] Brian G Demczyk, Yan Mei Wang, J Cumings, M Hetman, W Han, A Zettl, and RO Ritchie. Direct mechanical measurement of the tensile strength and elastic modulus of multiwalled carbon nanotubes. *Materials Science and Engineering: A*, 334(1-2):173–178, 2002.
- [5] Alan B Kaiser. Electronic transport properties of conducting polymers and carbon nanotubes. *Reports on Progress in Physics*, 64(1):1, 2001.
- [6] L.-C. Qin. Determination of the chiral indices (n,m) of carbon nanotubes by electron diffraction. *Phys. Chem. Chem. Phys.*, page 31–48, 2007.
- [7] L.-C. Qin. Electron diffraction from cylindrical nanotubes. *Journal of materials research*, 9(9):2450–2456, 1994.
- [8] L.-C. Qin. Electron diffraction from carbon nanotubes. *Reports on Progress in Physics*, 69(10):2761, 2006.
- [9] Francis Crick and James Watson. A structure for deoxyribose nucleic acid. *Nature*, 171(737-738):3, 1953.
- [10] Maurice Hugh Frederick Wilkins, Alex R STOKES, and Herbert R Wilson. Molecular structure of nucleic acids: molecular structure of deoxypentose nucleic acids. *Nature*, 171(4356):738–740, 1953.
- [11] Rosalind E Franklin and Raymond G Gosling. Molecular configuration in sodium thymonucleate. *Nature*, 171(4356):740–741, 1953.
- [12] AA Lucas, Vincent Bruyninckx, and Ph Lambin. Calculating the diffraction of electrons or x-rays by carbon nanotubes. *EPL (Europhysics Letters)*, 35(5):355, 1996.
- [13] G Dresselhaus, Saito Riichiro, et al. *Physical properties of carbon nanotubes*. World scientific, 1998.
- [14] Carlo Knupp and John Squire. Helix.
- [15] William Cochran, FH Crick, and Vladimir Vand. The structure of synthetic polypeptides. i. the transform of atoms on a helix. *Acta Crystallographica*, 5(5):581–586, 1952.
- [16] Amand A Lucas and Philippe Lambin. Diffraction by dna, carbon nanotubes and other helical nanostructures. *Reports on Progress in Physics*, 68(5):1181, 2005.
- [17] Lu-Chang Qin. Measuring the true helicity of carbon nanotubes. *Chemical physics letters*, 297(1-2):23–28, 1998.

- [18] Nicholas George and Shen-ge Wang. Neural networks applied to diffraction-pattern sampling. *Applied Optics*, 33(14):3127–3134, 1994.
- [19] Santosh K Suram, Yexiang Xue, Junwen Bai, Ronan Le Bras, Brendan Rappazzo, Richard Bernstein, Johan Bjorck, Lan Zhou, R Bruce van Dover, Carla P Gomes, et al. Automated phase mapping with agilefd and its application to light absorber discovery in the v–mn–nb oxide system. *ACS combinatorial science*, 19(1):37–46, 2017.
- [20] Jin-Woong Lee, Woon Bae Park, Jin Hee Lee, Satendra Pal Singh, and Kee-Sun Sohn. A deep-learning technique for phase identification in multiphase inorganic compounds using synthetic xrd powder patterns. *Nature Communications*, 11(1):1–11, 2020.
- [21] JA Aguiar, ML Gong, RR Unocic, T Tasdizen, and BD Miller. Decoding crystallography from high-resolution electron imaging and diffraction datasets with deep learning. *Science Advances*, 5(10):eaaw1949, 2019.
- [22] Artur Souza, Leonardo B Oliveira, Sabine Hollatz, Matt Feldman, Kunle Olukotun, James M Holton, Aina E Cohen, and Luigi Nardi. Deepfreak: Learning crystallography diffraction patterns with automated machine learning. *arXiv preprint arXiv:1904.11834*, 2019.
- [23] Jun-Tae Lee, Han-Ul Kim, Chul Lee, and Chang-Su Kim. Semantic line detection and its applications. In *Proceedings of the IEEE International Conference on Computer Vision*, pages 3229–3237, 2017.
- [24] Karen Simonyan and Andrew Zisserman. Very deep convolutional networks for large-scale image recognition. *arXiv preprint arXiv:1409.1556*, 2014.
- [25] Adam Paszke, Sam Gross, Francisco Massa, Adam Lerer, James Bradbury, Gregory Chanan, Trevor Killeen, Zeming Lin, Natalia Gimelshein, Luca Antiga, Alban Desmaison, Andreas Kopf, Edward Yang, Zachary DeVito, Martin Raison, Alykhan Tejani, Sasank Chilamkurthy, Benoit Steiner, Lu Fang, Junjie Bai, and Soumith Chintala. Pytorch: An imperative style, high-performance deep learning library. In H. Wallach, H. Larochelle, A. Beygelzimer, F. dAlché-Buc, E. Fox, and R. Garnett, editors, *Advances in Neural Information Processing Systems 32*, pages 8024–8035. Curran Associates, Inc., 2019.